9. M. G. Leakey, C. S. Feibel, I. McDougall, A. C. Walker, *Nature* **376**, 565 (1995).
10. T. D. White, G. Suwa, B. Asfaw, *ibid.* **371**, 306 (1994); *ibid.* **375**, 88 (1995).
11. A. T. Chamberlain and B. A. Wood, *J. Hum. Evol.* **16**, 119 (1987); R. R. Skelton and H. M. McHenry, *ibid.* **23**, 309 (1992); D. S. Strait, F. E. Grine, M. A. Moniz, *ibid.* **32**, 17 (1997); R. R. Skelton and H. M. McHenry, *ibid.* **34**, 109 (1997).
12. F. E. Grine, Ed., *Evolutionary History of "Robust" Australopithecines* (de Gruyter, New York, 1988); A. C. Walker, R. E. Leakey, J. M. Harris, F. H. Brown, *Nature* **322**, 517 (1986); H. M. McHenry, in *Contemporary Issues in Human Evolution*, W. E. Meikle, F. C. Howell, N. G. Jablonski, Eds. (California Academy of Sciences, San Francisco, 1996), pp. 77–92.
13. W. H. Kimbel, T. D. White, D. C. Johanson, *Am. J. Phys. Anthropol.* **64**, 337 (1984); G. Suwa *et al.*, *Nature* **389**, 489 (1997); P. V. Tobias, *Olduvai Gorge, Volume 4: The Skulls, Endocasts and Teeth of* Homo habilis (Cambridge Univ. Press, Cambridge, 1991).
14. W. H. Kimbel, D. C. Johanson, Y. Rak, *Nature* **368**, 449 (1994).
15. A. C. Walker and R. E. Leakey, Eds., *The Nariokotome* Homo erectus *Skeleton* (Harvard Univ. Press, Cambridge, MA, 1993).
16. Femur and humerus length were virtually complete in A.L. 288-1 [D. C. Johanson *et al.*, *Am. J. Phys. Anthropol.* **57**, 403 (1982)]. In BOU-VP-12/1, the femur is preserved from the intersection of the medial terminus of the neck with the (missing) femoral head (proximally) to a point on the medial supracondylar line just superior to the gastrocnemius impression (distally). This distance was measured in a sex- and species-balanced sample of *Pan*, *Gorilla*, and *Homo* ($N = 60$) and used to regress (least squares) femoral length [correlation coefficient (r^2) = 0.952; 95% confidence interval of estimate = ±0.28]. This regression computes the BOU-VP-12/1 femur at 348 mm. On anatomical grounds, we believe it to have actually been slightly shorter (about 335 mm). Much of the shaft of the BOU-12/1 humerus is preserved, including the point of confluence between the diaphysis and the medial epicondylar apophysis and the distalmost extent of the deltopectoral crest. This distance was used to regress humeral length with the same sample (length estimate = 226 mm; r^2 = 0.876; 95% confidence interval of estimate = ±0.40). On anatomical grounds, we estimate the humerus to have been slightly longer (about 236 mm). Radial length was estimated for A.L. 288-1 with multiple linear regressions from the same sample (breadth distal articular surface; maximum diameter radial head; length radial neck; r^2 = 0.929; 95% confidence interval of estimate = ±0.29) and for BOU-VP-12/1 (radial head to nutrient foramen; maximum diameter radial head; length radial neck; r^2 = 0.937; 95% confidence interval of estimate = ±0.27). These regressions estimate a length of 203 mm for A.L. 288-1 and 231 mm for BOU-VP-12/1. On anatomical grounds, the BOU-VP-12/1 estimate appears correct. However, we believe that the A.L. 288-1 radius is underestimated on the basis of a lack of sufficient "anatomical space" with which to accommodate all of the preserved pieces of the bone. A regression limited to a sample of common chimpanzees and bonobos ($N = 36$) estimates a length of 215 mm (r^2 = 0.529; 95% confidence interval of estimate = ±0.36). This result appears more probable. Only exceptionally pronounced errors in any of the above predictions would alter the conclusions made in the legend of Fig. 3, nor are these conclusions altered by regressions based only on single hominoid species.
17. The Middle Awash paleoanthropological project is multinational (13 countries), interdisciplinary research co-directed by B.A., Y. Beyene, J. D. Clark, T.W., and G. WoldeGabriel. The research reported here was supported by the NSF. We thank N. Tahiro and A. Abdo for their assistance in naming the new species. We thank Y. Haile-Selassie for discovery of the BOU-VP-12/130 holotype and H. Gilbert and D. DeGusta for field and illustrations work. R. Holloway kindly allowed us to cite his BOU-VP-12/130 cranial capacity estimate. L. Gudz made the palate and postcranial drawings. D. Brill made the photographs. P. Reno provided comparative primate

Electron Solvation in Finite Systems: Femtosecond Dynamics of Iodide·(Water)_n Anion Clusters

L. Lehr,*† M. T. Zanni,* C. Frischkorn, R. Weinkauf,†
D. M. Neumark‡

Electron solvation dynamics in photoexcited anion clusters of $I^-(D_2O)_{n=4-6}$ and $I^-(H_2O)_{4-6}$ were probed by using femtosecond photoelectron spectroscopy (FPES). An ultrafast pump pulse excited the anion to the cluster analog of the charge-transfer-to-solvent state seen for I^- in aqueous solution. Evolution of this state was monitored by time-resolved photoelectron spectroscopy using an ultrafast probe pulse. The excited $n = 4$ clusters showed simple population decay, but in the $n = 5$ and 6 clusters the solvent molecules rearranged to stabilize and localize the excess electron, showing characteristics associated with electron solvation dynamics in bulk water. Comparison of the FPES of $I^-(D_2O)_n$ with $I^-(H_2O)_n$ indicates more rapid solvation in the H_2O clusters.

A free electron can be trapped by solvent reorientation in polar solvents such as ammonia (*1*) or water (*2*). These "solvated" electrons play an important role in condensed phase chemistry, including radiation chemistry, electron transfer, and charge-induced reactivity. A microscopic understanding of the electron-solvent and solvent-solvent interactions that govern electron solvation is therefore a fundamental and challenging problem. These considerations have motivated femtosecond time-resolved studies that have demonstrated rich and complex dynamics after electronic excitation of electrons in water (*3, 4*).

To gain a complementary perspective on this problem, we studied solvated electron dynamics in finite clusters and compared these results with our understanding of bulk solvation phenomena. We used two-photon anion femtosecond (10^{-15} s) photoelectron spectroscopy (FPES) (*5, 6*) to study electron solvation dynamics in the mass-selected anion clusters $I^-(D_2O)_n$ and $I^-(H_2O)_n$ in order to address the following questions: (i) What

Department of Chemistry, University of California, Berkeley, CA 94720, USA and Chemical Sciences Division, Lawrence Berkeley National Laboratory, Berkeley, CA 94720, USA.

*These authors contributed equally to this work.
†Permanent address: Institut für Physikalische und Theoretische Chemie, Technische Universität München, D-85748 Garching, Germany.
‡To whom correspondence should be addressed. E-mail: dan@radon.cchem.berkeley.edu

is a minimum solvent cluster size needed to solvate an electron? (ii) What is a typical time scale for solvent reorientation in a cluster? (iii) What type of solvent motion is involved in electron solvation dynamics?

Aqueous solutions of I^- exhibit broad electronic bands in the ultraviolet (UV) corresponding to electron ejection from I^- into the solvent (*7*), known as "charge-transfer-to-solvent" (CTTS) states. Excitation of these states is an elegant means of generating solvated electrons, as was first demonstrated by Jortner (*8*). The dynamics of these states have been investigated by Eisenthal (*9*), Gaudeul (*10*), Bradforth (*11*), and their co-workers, all of whom excited the CTTS states to inject an electron into the water and then followed the subsequent electron solvation dynamics by femtosecond absorption spectroscopy. These experimental studies along with simulations by Sheu and Rossky (*12*) and Staib and Borgis (*13*) show that excitation of the lowest energy CTTS band results in the generation of fully solvated electrons on a 200-fs time scale (*11*). Once generated, these electrons thermalize with the solvent molecules, and some are then lost through geminate recombination with the neutral halogen atom over a time scale of tens of picoseconds.

The issue of how the CTTS bands manifest themselves in finite clusters was first addressed in experiments by Johnson and co-workers (*14*), in which a diffuse absorption band was seen just above the detachment

threshold for $I^-(H_2O)_n$ clusters ($n = 1$ to 4). As the number of water molecules increases, this band shifts to the blue and appears to converge toward the lower energy CTTS band in aqueous solution. These cluster analogs to the CTTS band most likely correspond to excitation of the electron from an orbital localized on the I^- into a more delocalized state supported by the network of water molecules in the cluster.

The work reported here builds on these spectroscopic measurements in that we use FPES to perform time-resolved measurements of the microscopic electron solvation dynamics subsequent to excitation of the CTTS cluster analog bands. In these experiments, mass-selected clusters of $I^-(H_2O)_n$ are electronically excited with a UV pump laser pulse (263 nm and 4.71 eV) of ~100 fs duration. The upper state evolves for a fixed time interval and is then photodetached by a probe laser pulse (790 nm and 1.57 eV) of similar duration. The resulting photoelectron (PE) spectrum provides a "snapshot" of the upper state. Measurement of the PE spectrum at a series of pump-probe delay times thus provides a detailed probe of

the electron and solvent dynamics in the electronically excited state. The overall experiment is described in detail elsewhere (5, 15, 16).

Results are presented here for $I^-(D_2O)_n$ and $I^-(H_2O)_n$ ($n = 4$ to 6). Our results suggest that for all the clusters, the electron is photoexcited into a dipole-bound state supported by the network of water molecules. In the $n = 4$ cluster, this state decays rapidly by vibrational autodetachment. However, the $n = 5$ and $n = 6$ clusters undergo solvent rearrangement that stabilizes the excess electron. These systems are therefore the smallest in which the cluster analog of electron solvation occurs.

FPE spectra for $I^-(D_2O)_{4-6}$ are shown in Fig. 1, A through C; those for $I^-(H_2O)_5$ are shown in Fig. 1D. Each plot shows a two-dimensional contour plot of PE intensity versus electron kinetic energy (eKE) and pump-probe delay. Figure 2 shows the average eKE as a function of time for these four clusters as well as for $I^-(H_2O)_4$ and $I^-(H_2O)_6$.

In the FPES of $I^-(D_2O)_4$ (Fig. 1A), the intensity rises to a maximum during the first 200 fs, and during this time the average eKE decreases by about 0.07 eV. By 200 fs, the spectrum is centered at 1.38 eV with a full width at half maximum (FWHM) of 0.28 eV. At longer times, the spectrum shifts slightly toward lower eKE (0.04 eV by 1 ps), but the major time-dependent effect observed is decay of the integrated intensity, dropping by about 20% over 2.3 ps.

The FPE spectra of the larger clusters are more complex. The eKEs stay constant for several hundred femtoseconds and then undergo significant shifts to lower eKEs. In addition, the intensity of the electron signal varies nonmonotonically with time. For $I^-(D_2O)_5$ (Fig. 2B), starting from 200 fs, the average eKE decreases from 1.38 to 1.17 eV, with a time constant of 390 fs. The contour plot shows the maximum electron intensity remaining constant until ~400 fs, after which it increases, reaching an absolute maximum by 2300 fs. At much longer pump-probe delays, the signal decays with a time constant of

about 37 ± 1 ps. The shift in eKE is accompanied by an increase in the overall width of the spectrum, from 0.27 eV at 180 fs to 0.34 eV at 800 fs. Similar trends are seen for $I^-(D_2O)_6$. The main differences are that the shift toward lower eKE (from 1.33 to 1.05 eV) is slower, with a time constant of 560 fs. The contour plot in Fig. 1 shows a slight dip in maximum intensity around 500 fs before rising at longer times. The signal ultimately decays with a time constant of 96 ± 3 ps.

Comparison of $I^-(D_2O)_n$ and $I^-(H_2O)_n$ results in Figs. 1 and 2 reveals the effects of isotopic substitution. The $I^-(H_2O)_n$ clusters are all shifted by 20 meV toward higher eKE, a shift attributed to zero-point energy effects. We find virtually no difference in the time evolution of the $n = 4$ clusters. For $n = 5$ and $n = 6$, the shift toward lower electron energy begins about 100 fs earlier in the H_2O clusters. The time constant for this shift is the same for the $n = 5$ clusters but is about 17% lower for $I^-(H_2O)_6$ (470 fs) than for $I^-(D_2O)_6$.

The most important feature of these results is the marked change in the time evolution of the spectra in going from the $n = 4$ to $n = 5$ clusters. The results suggest that simple population decay of an excited state occurs for $n = 4$, whereas for $n \geq 4$ a severe reorganization within the cluster must take place. The initial excitation and subsequent dynamics responsible for these effects are considered below.

Ground state structures for $X^-(H_2O)_{n\geq4}$ clusters have been calculated by Jortner and co-workers (17), Perera and Berkowitz (18), and Xantheas (19). These structures all show the halide bound to a water cluster, with the water molecules oriented so as to maximize their interaction with each other and with the halide anion. For example, in the solvent network for $I^-(H_2O)_4$, each water molecule binds to another with one hydrogen bond and simultaneously offers the other dangling hydrogen to the anion, to form a ring of water molecules, each with an H atom pointing toward the halide. As more waters are added, the I^- is predicted to remain on the "surface" of the water cluster, although this point is somewhat controversial [based on comparison with PE spectra of $I^-(H_2O)_n$ clusters obtained by Cheshnovsky and co-workers (17, 20)].

Johnson and co-workers have pointed out that the orientation of the water molecules induced by the halide results in a high dipole moment, estimated at $\mu = 4.4$ debye (D) for the water network in $I^-(H_2O)_4$, for example (14). Neutral molecules with a dipole moment larger than ≈ 2 D can bind an electron in a "dipole-bound" state (21)—the negative ion analog of a Rydberg state, in which the orbital for the excess electron is exceptionally diffuse. It is therefore reasonable to assign the upper state initially generated by the pump pulse to a short-lived state of the form $I(^2P_{3/2})\cdot(H_2O)_n{}^-$, in which the
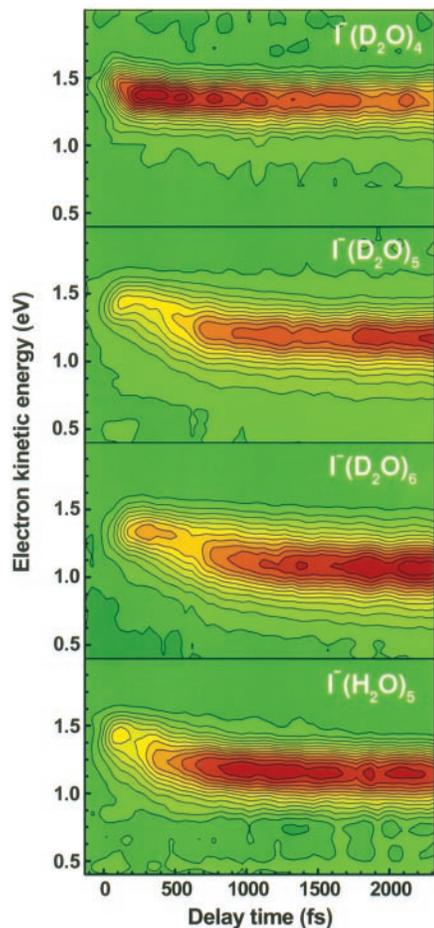
Fig. 1. Femtosecond PE spectra of (**A** through **C**) $I^-(D_2O)_n$ ($n = 4$ through 6) and (**D**) $I^-(H_2O)_5$ plotted as two-dimensional contour plots of eKE versus pump-probe delay time.
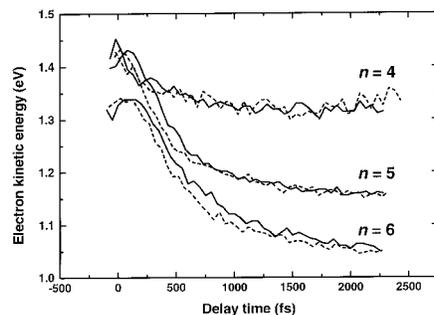
Fig. 2. Plot of average eKE as function of delay time for clusters shown in Fig. 1 as well as for $I^-(H_2O)_{4,6}$. Solid lines indicate D_2O clusters; dotted lines indicate H_2O clusters.

electron is transferred from the halide to a dipole-bound state of the solvent network.

The FPE spectra for $I^-(D_2O)_4$ and $I^-(H_2O)_4$ indicate that the initially excited electronic state undergoes population decay, with no other dynamics occurring. The pump photon energy, 4.71 eV, lies well above the adiabatic detachment energy of $I^-(D_2O)_4$, 4.36 eV (22), so decay of the excited state by electron emission is certainly energetically accessible. Moreover, the PE spectrum is centered at 1.38 eV, whereas the probe photon energy is 1.57 eV, so the vertical detachment energy for the excited state is 0.19 eV. Excitation at the pump wavelength thus results in an excited electronic state with ~0.45 eV of vibrational energy. We attribute the decay of this state to vibrational autodetachment to form $I(^2P_{3/2}) \cdot (D_2O)_4 + e^-$.

The time evolution of the FPES spectra for $n = 5$ and $n = 6$ clusters shows that complex dynamics occur after initial photoexcitation into the dipole-bound state. The lowering of the mean electron energy by ~0.3 eV during the first picosecond implies that the excess electron is stabilized by solvent motion on this time scale. Moreover, the nonmonotonic variation of integrated electron intensity suggests that the nature of the orbital in which the excess electron resides changes significantly over the time scale of this intensity variation. Overall, we attribute these trends to solvent isomerization from the initial dipole-bound state to a second more stable conformer with the character of a partially solvated electron.

Figure 3 presents a qualitative potential energy surface diagram consistent with our results for the $n = 5$ and $n = 6$ clusters. The dipole-bound state discussed above is resonantly excited by the pump pulse at 263 nm, and subsequent dynamics are probed by photodetachment with the time-delayed probe pulse at 790 nm. As shown by Bowen and co-workers (23), photodetachment of a dipole-bound state results in minimal Franck-Condon activity, which is consistent with the narrow width of the PE spectrum at short delay times. If isomerization into a lower energy cluster conformer then occurs, electronic energy is converted into vibrational energy. For a cluster of this size, this vibrational energy should be dispersed over many vibrational modes. The relatively small broadening accompanying the electron energy shift indicates only slightly more Franck-Condon activity in the partially solvated state than in the initially excited state. Thus, the excess vibrational energy of this state largely remains as vibrational energy upon photodetachment, so the 0.3-eV shift of the eKE is approximately equal to the difference in the vertical detachment energies of the conformers.

The time-dependent intensities for the $n = 5$ and $n = 6$ clusters (Fig. 1) cannot be attributed to the population of excited-state anions, as this must decline monotonically once the pump

pulse terminates. Instead, it appears that the dynamics associated with stabilization of the excess electron also result in an increased photodetachment cross-section. This result is consistent with isomerization from a dipole-bound state, in which the electron cloud is exceedingly diffuse, to a conformer in which the excess electron is more solvated and hence more localized. Two isomers are known to exist for $(H_2O)_6^-$, and the photodetachment cross-section for the more weakly bound isomer (with respect to electron detachment) is considerably less than for the more strongly bound isomer (24). The vertical detachment energies for these isomers (0.2 and 0.5 eV) are quite close to those for the two excited $I^-(H_2O)_6$ species in our experiment.

We next consider isotopic effects. The earlier onset (by 100 fs) of the shift in electron energy for $I^-(H_2O)_5$ and $I^-(H_2O)_6$ as compared to that of the analogous D_2O clusters indicates that isomerization begins earlier in the H_2O clusters, and suggests that librational-rotational motion of the solvent molecules plays an important role in stabilizing the excess electron. A large isotope effect attributed to librational solvent motion has also been seen at very early times (30 to 80 fs) in bulk hydrated electron studies (4).

Figure 4 presents a qualitative picture of the isomerization and electronic localization dynamics that is consistent with our experimental results. At short delay times, the geometry of the initially excited state (Fig. 4B) should resemble that of the ground state (Fig. 4A) (17), and the excess electron in Fig. 4B is bound by the dipole moment of the solvent network. However, Kim and co-workers (25) calculate that the lowest energy structure for $(H_2O)_6^-$ is quite different from the solvent network in Fig. 4B; they find instead a "half-cage" structure in which the excess electron is considerably more localized. Their calculation is the basis for the structure in Fig. 4C, which has a different hydrogen bonding network than that in Fig. 4B.

One must realize the approximate nature of Fig. 4. First, because of the finite (and unknown) cluster temperature, it is possible that fluctional as well as rigid structures play a role in the dynamics. For example, recent infrared (IR) spectroscopy experiments on $I^-(H_2O)_2$ suggest that the interwater hydrogen bond is disrupted at finite temperatures (26). In addition, many low-lying isomers are expected for $(H_2O)_6^-$ (25), including a linear structure that appears to be consistent with its IR spectrum (27). Finally, perturbations and

Fig. 3. Excitation scheme of resonant UV-IR two-photon photodetachment via dipole-bound states. Front plane: anion states. Rear gray plane: neutral states. (**A**) Pump-probe excitation via dipole-bound states. (**B**) Isomerization to a lower energetic conformer. The electronic energy converted into vibration is no longer fully available for the photodetachment, resulting in a red shift of PE energy.
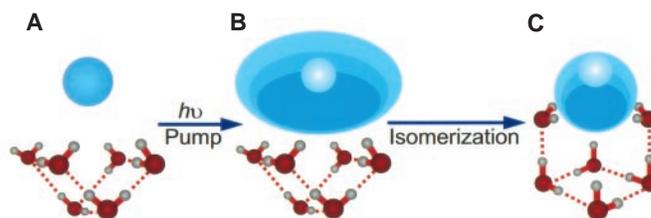
Fig. 4. Candidate structures for (**A**) ground state, (**B**) dipole-bound excited state, and (**C**) partially solvated state of $I^-(H_2O)_6$. (A) and (B) are based on the anion ground state calculated in (17), and (C) is based on the lowest energy calculated structure for $H_2O_6^-$ (25).

dynamics associated with the neutral I atom have not been considered.

We close by comparing our results to Bradforth's experiments (*11*) on CTTS excitation of I⁻ in liquid water, because these are the liquid-phase experiments most analogous to ours. In his experiments, transient absorption at 800 nm was monitored after excitation at 255 nm. Bradforth observed a short-lived (~50 fs) transient assigned to the initially excited CTTS state, followed by an increasing absorption with a rise time of 200 fs associated with formation of the solvated electron; this then decayed biexponentially with time constants of 9 and 60 ps. This interpretation suggests several parallels with the $n = 5$ and $n = 6$ FPES results presented here; namely that the CTTS state in the bulk is analogous to the short-lived dipole-bound state seen in our experiments, and that the bulk solvation on a 200-fs time scale corresponds to the isomerization and solvation dynamics in our experiments. There are, however, important differences. Simulations of CTTS excitation show that solvation is accompanied by the electron moving away from the halogen species (*12, 13*), which is a reasonable result for an infinite number of water molecules but may not occur in a small cluster. Also, in liquid water, the longer time decay of the solvated electron signal occurs by recombination with neutral I atoms. Although this may be responsible for the long time decay in the clusters, a likelier mechanism is thermionic emission, which generally does not occur in liquids.

References and Notes

1. W. Weyl, *Poyg. Ann.* **123**, 350 (1864).
2. E. J. Hart and J. W. Boag, *J. Am. Chem. Soc.* **84**, 4090 (1962).
3. M. Wiesenfeld and E. P. Ippen, *Chem. Phys. Lett.* **73**, 47 (1980); A. Migus, Y. Gauduel, J. L. Martin, A. Antonetti, *Phys. Rev. Lett.* **58**, 1559 (1987).
4. C. Silva, P. K. Walhout, K. Yokoyama, P. F. Barbara, *Phys. Rev. Lett.* **80**, 1086 (1998).
5. B. J. Greenblatt, M. T. Zanni, D. M. Neumark, *Chem. Phys. Lett.* **258**, 523 (1996).
6. B. J. Greenblatt, M. T. Zanni, D. M. Neumark, *Science* **276**, 1675 (1997).
7. J. Franck and G. Scheibe, *Z. Phys. Chem. A* **139**, 22 (1928).
8. J. Jortner, M. Ottolenghi, G. Stein, *J. Phys. Chem.* **68**, 247 (1964).
9. F. H. Long, X. Shi, H. Lu, K. B. Eisenthal, *ibid.* **98**, 7252 (1994).
10. Y. Gaudeul, H. Gelabert, M. Ashokkumar, *Chem. Phys.* **197**, 167 (1995).
11. J. A. Kloepfer, V. H. Vilchiz, V. A. Lenchenkov, S. E. Bradforth, *Chem. Phys. Lett.* **298**, 120 (1998).
12. W.-S. Sheu and P. J. Rossky, *ibid.* **213**, 233 (1993).
13. A. Staib and D. Borgis, *J. Chem. Phys.* **104**, 9027 (1996).
14. D. Serxner, C. E. Dessent, M. A. Johnson, *ibid.* **105**, 7231 (1996).
15. B. J. Greenblatt, M. T. Zanni, D. M. Neumark, *Disc. Faraday Soc.* **108**, 101 (1997).
16. Briefly, a pulsed beam of cold I⁻(D₂O)ₙ anion clusters is formed by crossing an electron beam with a pulsed supersonic expansion of a gas mixture of about 5% CH₃I and 2% D₂O (or H₂O) in 1 bar N₂ into a vacuum chamber. The resulting anions are mass selected by time of flight and interact with the pump and probe laser pulses at the focus of a "magnetic bottle" time-of-flight PE spectrometer. The pump and probe laser pulses were generated by a Ti:sapphire oscillator-regenerative amplifier system (Clark MXR) running at a repetition rate of 500 Hz.
17. J. E. Combariza, N. R. Kestner, J. Jortner, *J. Chem. Phys.* **100**, 2851 (1994); *Chem. Phys. Lett.* **221**, 156 (1994).
18. L. Perera and M. Berkowitz, *J. Chem. Phys.* **100**, 3085 (1994).
19. S. S. Xantheas, *J. Phys. Chem.* **100**, 9703 (1996).
20. G. Markovich, S. Pollack, R. Giniger, O. Cheshnovsky, *J. Chem. Phys.* **101**, 9344 (1994).
21. O. H. Crawford, *Mol. Phys.* **20**, 585 (1971).
22. T. R. Taylor, H. Gomez, D. M. Neumark, in preparation.
23. J. V. Coe *et al.*, *J. Chem. Phys.* **92**, 3980 (1990); J. H. Hendricks *et al.*, in *Structure and Dynamics of Clusters*, T. Kondow, K. Kaya, A. Terasaki, Eds. (Universal Academy Press, Tokyo, 1996), pp. 321–328.
24. C. G. Bailey and M. A. Johnson, *Chem. Phys. Lett.* **265**, 185 (1997).
25. S. Lee, J. Kim, S. J. Lee, K. S. Kim, *Phys. Rev. Lett.* **79**, 2038 (1997).
26. P. Ayotte *et al.*, *Chem. Phys.* **239**, 485 (1998).
27. P. Ayotte *et al.*, *J. Chem. Phys.* **110**, 6268 (1999).
28. Supported by the Air Force Office of Scientific Research under grant F49620-97-0018. R.W. acknowledges funding by the Deutsche Forschungsgemeinschaft. C.F. acknowledges postdoctoral support from the Deutsche Akademie der Naturforscher Leopoldina (grant BMBF-LPD 9801-6). L.L. acknowledges financial support by E. W. Schlag.

Requirement for Tec Kinases Rlk and Itk in T Cell Receptor Signaling and Immunity

Edward M. Schaeffer,[1]* Jayanta Debnath,[1,2]*† George Yap,[3] Daniel McVicar,[2] X. Charlene Liao,[4] Dan R. Littman,[5] Alan Sher,[3] Harold E. Varmus,[2] Michael J. Lenardo,[3] Pamela L. Schwartzberg[1,2]‡

T cell receptor (TCR) signaling requires activation of Zap-70 and Src family tyrosine kinases, but requirements for other tyrosine kinases are less clear. Combined deletion in mice of two Tec kinases, Rlk and Itk, caused marked defects in TCR responses including proliferation, cytokine production, and apoptosis in vitro and adaptive immune responses to *Toxoplasma gondii* in vivo. Molecular events immediately downstream from the TCR were intact in $rlk^{-/-}itk^{-/-}$ cells, but intermediate events including inositol trisphosphate production, calcium mobilization, and mitogen-activated protein kinase activation were impaired, establishing Tec kinases as critical regulators of TCR signaling required for phospholipase C–γ activation.

Stimulation of T lymphocytes through the TCR elicits broad responses required for proper immune function, including cell proliferation, cytokine production, and apoptosis. Key components of TCR signaling are nonreceptor tyrosine kinases, and cells lacking Lck or Zap-70 are essentially unresponsive to antigen (*1, 2*). The Tec kinases, exemplified by BTK, are a distinct family with members specifically expressed in lymphoid lineages (*3, 4*). *BTK* mutations cause severe immunodeficiencies, with defective B cell development and function (*4*). No disease is yet associated with the loss of Tec kinases in T lymphocytes, which express Itk, Rlk, and Tec (*3*). Itk-deficient mice have only mildly impaired responses to infection (*5*), suggesting functional redundancy between these kinases.

Rlk (also called Txk) is a Tec kinase expressed in developing and mature T lymphocytes (*6*). Rlk resembles other Tec kinases in that it lacks the COOH-terminal regulatory tyrosine and myristoylation sequences of Src kinases, has a proline-rich region that binds SH3 domains, and is activated by phosphorylation by Src kinases. However, Rlk lacks the phosphatidylinositol phosphate–binding pleckstrin homology domain common to other Tec kinases and is activated independently of phosphoinositide 3-kinase (PI3K) activity. Instead, Rlk has a palmitoylated cysteine-string motif, required for subcellular localization (*7*). To better understand the contribution of Tec kinases to T cell signaling, we analyzed mice mutated in Rlk, Itk, or both kinases.

Because alternate translation initiation generates at least two Rlk isoforms, a full-length protein and a shorter species lacking the cysteine string (*7*), we introduced a targeted mutation downstream of the second

[1]National Human Genome Research Institute, [2]National Cancer Institute, [3]National Institute for Allergy and Infectious Diseases, NIH, Bethesda, MD 20892, USA. [4]Tularik, 2 Corporate Drive, South San Francisco, CA 94080, USA. [5]Skirball Institute of Biomolecular Medicine, NYU Medical Center, 540 First Avenue, New York, NY 10016, USA.

*These authors contributed equally to this work.
†Present address: Department of Pathology, Brigham and Women's Hospital, 75 Francis Street, Boston, MA 02115, USA.
‡To whom correspondence should be addressed. E-mail: pams@nhgri.nih.gov